ISSN 1674-1056
http://cpb.iphy.ac.cn
http://iopscience.iop.org/cpb
中国物理 B
Chinese Physics
中国物理 Chinese Physics B

Comparative study of photoionization of atomic hydrogen by solving the one- and three-dimensional time-dependent Schrödinger equations

Shun Wang(王顺), Shahab Ullah Khan, Xiao-Qing Tian(田晓庆), Hui-Bin Sun(孙慧斌), and Wei-Chao Jiang(姜维超)

Citation: Chin. Phys. B, 2021, 30 (**8**): 083301. DOI: 10.1088/1674-1056/abea85
Journal homepage: http://cpb.iphy.ac.cn; http://iopscience.iop.org/cpb

What follows is a list of articles you may be interested in

Coulomb exploded directional double ionization of N_2O molecules in multicycle femtosecond laser pulses

Junyang Ma(马俊杨), Kang Lin(林康), Qinying Ji(季琴颖), Wenbin Zhang(张文斌), Hanxiao Li(李韩笑), Fenghao Sun(孙烽豪), Junjie Qiang(强俊杰), Peifen Lu(陆培芬), Hui Li(李辉), Xiaochun Gong(宫晓春), Jian Wu(吴健)
Chin. Phys. B, 2019, 28 (**9**): 093301. DOI: 10.1088/1674-1056/ab38aa

Effect of laser polarization on strong-field ionization and fragmentation of nitrous oxide molecules

Rui Wang(王瑞), Shi-Wen Zhang(张世文), Yang Liu(刘洋), Tian Sun(孙添), Hang Lv(吕航), Hai-Feng Xu(徐海峰)
Chin. Phys. B, 2019, 28 (**5**): 053301. DOI: 10.1088/1674-1056/28/5/053301

Enhanced ionization of vibrational hot carbon disulfide molecules in strong femtosecond laser fields

Wan-Long Zuo(左万龙), Hang Lv(吕航), Hong-Jing Liang(梁红静), Shi-Min Shan(单石敏), Ri Ma(马日), Bing Yan(闫冰), Hai-Feng Xu(徐海峰)
Chin. Phys. B, 2018, 27 (**6**): 063301. DOI: 10.1088/1674-1056/27/6/063301

Ellipticity-dependent ionization/dissociation of carbon dioxide in strong laser fields

Zhang Jun-Feng, Ma Ri, Zuo Wan-Long, Lv Hang, Huang Hong-Wei, Xu Hai-Feng, Jin Ming-Xing, Ding Da-Jun
Chin. Phys. B, 2015, 24 (**3**): 033302. DOI: 10.1088/1674-1056/24/3/033302

Imprints of molecular orbitals using photoelectron angular distribution by strong laser pulses of circular polarization

Ren Xiang-He, Zhang Jing-Tao, Wu Yan, Ma Hui, Xu Yu-Long
Chin. Phys. B, 2013, 22 (**7**): 073304. DOI: 10.1088/1674-1056/22/7/073304

Comparative study of photoionization of atomic hydrogen by solving the one- and three-dimensional time-dependent Schrödinger equations*

Shun Wang(王顺), Shahab Ullah Khan, Xiao-Qing Tian(田晓庆), Hui-Bin Sun(孙慧斌), and Wei-Chao Jiang(姜维超)†

College of Physics and Optoelectronic Engineering, Shenzhen University, Shenzhen 518060, *China*

(Received 26 November 2020; revised manuscript received 8 February 2021; accepted manuscript online 1 March 2021)

We develop a numerical scheme for solving the one-dimensional (1D) time-dependent Schrödinger equation (TDSE), and use it to study the strong-field photoionization of the atomic hydrogen. The photoelectron energy spectra obtained for pulses ranging from XUV to near infrared are compared in detail to the spectra calculated with our well-developed code for accurately solving the three-dimensional (3D) TDSE. For XUV pulses, our discussions cover intensities at which the ionization is in the perturbative and nonperturbative regimes. For pulses of 400 nm or longer wavelengths, we distinguish the multiphoton and tunneling regimes. Similarities and discrepancies between the 1D and 3D calculations in each regime are discussed. The observed discrepancies mainly originate from the differences in the transition matrix elements and the energy level structures created in the 1D and 3D calculations.

Keywords: time-dependent Schrödinger equation (TDSE), strong-field ionization, photoelectron spectra, dynamic interference

PACS: 33.20.Xx, 32.80.Rm, 42.65.Re **DOI:** 10.1088/1674-1056/abea85

1. Introduction

In the past few decades, nonlinear quantum processes stimulated by strong laser fields in atoms, molecules, and even solids and liquids, have been one of the central parts of the modern study of light–matter interactions.[1–3] The representative nonlinear processes include nonsequential double ionization,[4–6] high-order harmonic generation (HHG),[7–10] and dynamic interference (DI) in atomic ionization.[11–14] To fully understand these strong-field phenomena, not only sophisticated experimental technologies are required, but state-of-the-art numerical methods are also indispensable. The most accurate way to numerically reproduce the experimental data is, of course, performing calculations from first principles, i.e., directly solving the full-dimensional (FD) time-dependent Schrödinger equation (TDSE) that strictly describes the time-dependent system. This approach, on the one hand, has served as an important tool in strong-field physics over years and shown its power numerous times in the past numerical studies. On the other hand, however, it also has a serious drawback that the computational cost is often too large, which hinders its effectiveness under many circumstances.

To circumvent the aforementioned numerical difficulty, instead of solving the TDSE in its full dimensionality, one often solve it in reduced dimensions.[15,16] Reduced-dimensional (RD) TDSE is much more computationally tractable, but can still grasp the key physics in a lot of cases. For linearly (circularly) polarized pulses, the main dynamics happens along the polarization axis (in the polarization plane) and, therefore, the other two (one) dimensions can be approximately ignored. If one just needs to study the key physics rather than establish quantitatively exact correspondence between simulations and experiments, solving the RD TDSE is a rather good choice. In fact, quite a large number of fabulous works in strong-field physics have been based on the solution of the RD TDSE. For example, the 1D TDSE has been successfully applied to the studies of the resonance-like enhancements occurring in the plateau regions of the electron spectra for ionization of inertia gases by strong infrared pulses,[17] complex fine structures of the above-threshold-ionization spectra generated by the combination of Freeman resonances and quantum interferences,[18] and plasma currents induced via resonant destabilization of atoms.[16] Typical examples of the successful utilization of the 2D TDSE include investigations of the double ionization of helium,[19] ionization and tunneling times in HHG,[20] and nondipole effects in atomic ionization.[21,22]

In 1D TDSE calculations, simply using the Coulomb potential will cause numerical instability and give infinite ground state energy. Proper choice of the 1D model potential is essential and has been studied by many authors. A number of 1D potentials have been designed, such as the one-

*Project supported by the National Natural Science Foundation of China (Gant Nos. 12074265, 11804233, and 11575118), the National Key Research and Development Project of China (Grant No. 2017YFF0106500), the Natural Science Foundation of Guangdong, China (Grant Nos. 2018A0303130311 and 2021A1515010082), and the Shenzhen Fundamental Research Program (Grant Nos. KQJSCX20180328093801773, JCYJ20180305124540632, and JCYJ20190808121405740).

†Corresponding author. E-mail: jiang.wei.chao@szu.edu.cn

© 2021 Chinese Physical Society and IOP Publishing Ltd

sided hydrogenic potential,[23] the soft-core potential,[23] the Dirac delta potential,[24] the pliant-, solid- and supersolid-core potentials,[25] and the density-based model potential.[26] The commonly used soft-core potential eliminates the singularity of the Coulomb potential at the origin, but keeps the Coulomb tail at the far end and therefore supports the Rydberg series in the eigenspectrum. However, it was found that the singularity or at least a cusp of the potential is essential for calculations of the HHG spectra.[27] In this spirit, several 1D potentials which are more realistic for HHG were put forward.[25,26] We note that, influences of the chosen model potential have been extensively studied in the context of HHG, but much fewer authors[28,29] have studied the influences on photoionizations.

Despite its shortcomings, the soft-core potential is still the most widely used model potential in the 1D TDSE calculations. To examine to what extent the 1D calculations adopting the soft-core potential can reproduce the accurate results from the 3D TDSE calculations, it is necessary to make comparisons between the 1D and 3D results. Such comparisons can be commonly found in previous works on HHG.[26,30,31] However, comparisons between the 1D and 3D calculations of photoionizations are much less commonly seen. Some papers[32,33] focusing on specific physics compared the 1D and 3D results just to prove the validity of the 1D calculations for problems under discussion. For example, in Ref. [32], which focused on enhanced ionization in linear polyatomics, ionization rates of H_3^{2+} as a function of the internuclear distance from the 1D and 3D TDSE calculations were compared. Although the 1D calculation overestimated the ionization rate, it correctly gave the distance at which the ionization rate peaked, showing that the 1D calculation was valid for studying enhanced ionization. To our knowledge, a detailed systematic comparison between the 1D and 3D calculations, which covers various laser parameters, is rarely seen in the field of strong-field photoionization. In the present work, we develop a scheme for efficiently solving the 1D TDSE (with the soft-core potential). We then use this scheme and our existing, well-tested code for solving the 3D TDSE, to comparatively study the photoionization of atomic hydrogen. For several typical laser pulses, a systematic comparison of the photoelectron energy spectra from the 1D and 3D calculations is provided.

The paper is organized as follows. In Section 2, we first describe our scheme for solving the 1D TDSE in some detail and then briefly introduce our well developed numerical scheme for the solution of the 3D TDSE. In Section 3, numerical results are presented. A summary is given in the last section. We will use atomic units throughout unless otherwise stated.

2. Methods

2.1. The 1D TDSE calculation

In this work, we only use sine-squared laser pulses. The 1D TDSE to be solved is of the form

$$\mathrm{i}\frac{\partial}{\partial t}\psi(x,t)=\left[-\frac{1}{2}\frac{\partial^2}{\partial x^2}+V(x)+W(x,t)\right]\psi(x,t). \tag{1}$$

Here, $W(x,t)$ represents the electron-laser interaction under the dipole approximation. In the velocity gauge, $W(x,t)=-\mathrm{i}A(t)\frac{\partial}{\partial x}$, with $A(t)$ being the vector potential of the laser field. In the length gauge, $W(x,t)=xF(t)$, where $F(t)$ is the electric field the electron feels. $V(x)=-1/\sqrt{x^2+\alpha}$ is the soft-core Coulomb potential with an adjustable parameter α. The ground state energy of the field-free atomic Hamiltonian, $H_\mathrm{a}=-\frac{1}{2}\frac{\partial^2}{\partial x^2}+V(x)$, can be adjusted by varying α. When $\alpha=0$, the ground state energy is negatively infinite and all other bound states are two-fold degenerate; after removal of the ground state, the eigenspectrum is exactly the same as that of the 3D hydrogen.[34,35] When $\alpha=2$, the ground state energy exactly equals 0.5 a.u.,[26] thus representing the ground state atomic hydrogen. Furthermore, in this special case, the ground state wavefunction can be analytically obtained, which reads[26]

$$\psi_\mathrm{g}^\mathrm{H}(x)=N(1+\sqrt{x^2+2})\mathrm{e}^{-\sqrt{x^2+2}}, \tag{2}$$

where $N\approx 0.9748$ is the normalization factor.

The spatial coordinate x is discretized uniformly, with the spatial derivatives being represented by the finite difference approximations. Depending on the specific numerical scheme, we choose the three- or five-point central finite differentiation. Using more points to represent a spatial derivative brings about higher accuracy and, consequently, less spatial grids (i.e., larger grid spacing Δx) are required to achieve convergence in the TDSE calculation. However, using more points also consumes more computational time to calculate one derivative. In practical calculations, one needs to make a trade-off between the benefits and drawbacks of the chosen finite difference scheme.

The initial state, usually chosen as the ground state, should be calculated numerically, except for atomic hydrogen whose ground state is analytically obtainable. We calculate it by the direct diagonalization of the field-free atomic Hamiltonian, or with imaginary time evolution method. In the latter method, the time t in the real time evolution operator $\mathrm{e}^{-\mathrm{i}\hat{H}t}$ is replaced by the imaginary time $-\mathrm{i}\tau$, thus resulting in the imaginary time evolution operator $\mathrm{e}^{-\hat{H}\tau}$. Applying this operator on an arbitrary state $|\psi\rangle$, which can be expanded in terms of the eigenstates $|n\rangle$ $(n=0,1,2,\ldots)$ as

$$|\psi\rangle=\sum_n c_n|n\rangle, \tag{3}$$

one has

$$e^{-\hat{H}\tau}|\psi\rangle = e^{-E_0\tau}\left[\sum_{n\neq 0} c_n|n\rangle e^{-(E_n-E_0)\tau} + c_0|0\rangle\right]. \quad (4)$$

As τ increases, all terms in the summation $\sum_{n\neq 0}$ will decay. For sufficiently large τ, only the $|0\rangle$ term, i.e., the ground state, survives. To obtain the first excited state, one can subtract the ground state component from $|\psi\rangle$, and then apply the imaginary time evolution operator on the residual state $\sum_{n\neq 0} c_n|n\rangle$. Similarly, the i-th excited state is obtained by applying the operator on $\sum_{n\geqslant i} c_n|n\rangle$.

The time-evolution of the wavefunction $\psi(x,t)$ is realized using the Lanczos propagator or the fourth-order Runge–Kutta algorithm. A major difference between the two propagators is that the former keeps the unitarity of the time evolution operator whereas the latter does not. Practical calculations show that the former propagator is of higher efficiency, requiring larger time step Δt.

Once the final electron wavefunction $|\psi(t_f)\rangle$ is obtained, we use three different methods to calculate the energy distribution of the ionized electrons, $g(E)$. The first method is the most straightforward one, in which $g(E)$ is obtained by projecting the final wavefunction onto the continuum eigenstates of the field-free Hamiltonian, $|E\rangle$, i.e., $g(E) = |\langle E|\psi(t_f)\rangle|^2$. Alternatively, based on the continuum eigenstates $|E\rangle$, one can appropriately construct the scattering states, $|\phi_p\rangle$, which asymptotically approaches the plane wave with the momentum of p at infinity. Then, the momentum distribution of the ionized electrons, $f(p)$, is obtained as $f(p) = |\langle\phi_p|\psi(t_f)\rangle|^2$. The energy spectrum can be converted from the momentum spectrum by using the relation $g(E) = \frac{f(p)+f(-p)}{p}$. As far as we know, calculation of the spectra by projecting the wavefunction to the scattering state in the 1D TDSE simulation has not been reported before. The third method also converts the energy spectrum from the momentum spectrum using the above relation, but it calculates $f(p)$ by projecting $|\psi(t_f)\rangle$ onto the plane wave with momentum p, rather than onto the scattering state. Considering the asymptotic behavior of the scattering state, to accurately calculate the spectrum, one should allow the electron wavefunction to propagate under the field-free Hamiltonian for sufficiently long time after the laser pulse is turned off. The first method calculates the energy spectrum very accurately, however, it cannot calculate the momentum distribution. Another limitation of the first method is that it cannot avoid using large spatial box, especially when the pulse is long and intense. By contrast, in the other two methods, the momentum spectrum can be obtained straightforwardly, and, one can take advantage of the wave splitting technology, which will be explained latter, to avoid the use of very large spatial box. However, when the wave splitting technology is used, the third method encounters a new problem: for infrared pulses, the excited states, which are not orthogonal to the plane wave, are often populated and included in the final wavefunction; to correctly calculate the spectrum, the time of free propagation should be very long, apparently increasing the computational cost. Such a problem does not exist in the second method, since the excited states are orthogonal to the scattering state. Based on the above discussion, we can make a conclusion that the second method, which utilizes the scattering state, has great advantages over the other two methods.

As the electron wavepacket evolves with time, its spatial extension becomes larger. The simulation box should be sufficiently large to include the whole wavepacket, otherwise reflection would happen at the boundaries. However, the larger the simulation box, the more computationally demanding the simulation. In the case of intense and long laser pulses, the computational cost could be very huge. To circumvent this trouble, we adopt the powerful wave-splitting technology.[36] This technology splits the wavefunction into the inner part and the outer part, and propagates the two parts separately.

The wavefunction is split at specific equally spaced times t_i ($i = 1,2,3,\ldots$). At the first split, i.e., at t_1, the whole wavefunction $\psi(x,t_1)$ is split as

$$\begin{aligned}\psi(x,t_1) &= \psi^1_{\rm in}(x,t_1) + \psi^1_{\rm out}(x,t_1),\\ &= \psi(x,t_1)F_{\rm s}(x) + \psi(x,t_1)[1-F_{\rm s}(x)],\end{aligned} \quad (5)$$

where $\psi^1_{\rm in}(x,t_1)$ and $\psi^1_{\rm out}(x,t_1)$ stand for the wavefunctions in the inner region and the outer region, respectively. $F_{\rm s}(x) = 1/[1+e^{(|x|-x_{\rm c})/\Delta}]$ is a smoothed step function, with Δ representing the width of the crossover region. After the first split, $\psi^1_{\rm in}(x,t_1)$ is propagated rigorously according to the TDSE [Eq. (1)], whereas $\psi^1_{\rm out}(x,t_1)$ is propagated under the Volkov Hamiltonian, $H_{\rm V} = -\frac{1}{2}\frac{\partial^2}{\partial x^2} + W(x,t)$. This treatment is valid because, in the outer region, the Coulomb interaction is much weaker in comparison with the electron-laser coupling and can thus be overlooked. At the second split time t_2, the inner wavefunction generated at t_1, $\psi^1_{\rm in}(x,t_1)$, has evolved into $\psi^1_{\rm in}(x,t_2)$, which is not localized in the inner region anymore. In the same way, $\psi^1_{\rm in}(x,t_2)$ can be split into the inner part and the outer part as $\psi^1_{\rm in}(x,t_2) = \psi^2_{\rm in}(x,t_2) + \psi^2_{\rm out}(x,t_2)$. Thus, at the i-th split, the wavefunction is split as $\psi^{i-1}_{\rm in}(x,t_i) = \psi^i_{\rm in}(x,t_i) + \psi^i_{\rm out}(x,t_i)$. The momentum distribution $f(p)$ is obtained as follows. At the i-th split, the outer wavefunction $\psi^i_{\rm out}(x,t_i)$ is projected onto the plane wave or the scattering state to calculate the projection amplitude $C'(p,t_i)$. Then, from t_i to t_{i+1}, the above amplitude is changed only by multiplying a Volkov phase factor $U_p(t_i,t_{i+1}) = \exp\{-i\int_{t_i}^{t_{i+1}}[\frac{p^2}{2} + A(\tau)p]d\tau\}$. Thus, at t_i, the total amplitude is $C(p,t_i) = U_p(t_{i-1},t_i)C(p,t_{i-1}) + C'(p,t_i)$, where $C(p,t_{i-1})$ is the total amplitude at t_{i-1}. If projection onto the scattering state is adopted, at the final time t_f, no splitting is needed, and the new produced amplitude $C'(p,t_f)$ is obtained by projecting the whole residual wavefunction onto the

scattering state. However, if projection onto the plane wave is adopted, at t_f, splitting is still needed, in order to remove the bound state components which are not orthogonal to the plane wave. Eventually, the momentum distribution is obtained as $f(p) = |C(p,t_f)|^2$.

2.2. The 3D TDSE calculation

Our numerical code for solving the 3D TDSE is very well developed and has been used with considerable success in dealing with many problems.[12,37,38] Here, we just give a brief description of the method. The 3D TDSE to be solved reads

$$i\frac{\partial}{\partial t}\psi(\boldsymbol{r},t) = \left[-\frac{1}{2}\nabla^2 + V(r) + W(\boldsymbol{r},t)\right]\psi(\boldsymbol{r},t), \quad (6)$$

where $V(\boldsymbol{r}) = -1/r$ is the real 3D Coulomb potential, and $W(\boldsymbol{r},t)$ takes the form $-i\boldsymbol{A}(t)\cdot\nabla$ and $\boldsymbol{r}\cdot\boldsymbol{F}(t)$ in the velocity gauge and the length gauge, respectively. To solve the 3D TDSE, we first express the wavefunction as an expansion in spherical harmonics series,

$$|\psi(\boldsymbol{r},t)\rangle = \sum_{lm}\frac{R_{lm}(r,t)}{r}|lm\rangle, \quad (7)$$

so that the 3D equation is simplified to a 1D radial equation. The radial coordinate r is discretized using finite-element discrete variable representation (FE-DVR) method.[39–41] The recently proposed split-Lanczos propagator[42] is adopted for the time evolution of the wavefunction. As has been demonstrated,[42] this propagator greatly improves the efficiency of the traditional Lanczos propagator by splitting out the centrifugal potential from the whole Hamiltonian. To avoid using large radial box, our 3D method also adopts the wave-splitting technique.

The momentum distribution of the ionized electrons is calculated by projecting the final wavefunction onto the scattering state, as

$$f(\boldsymbol{p}) = |\langle\phi_{\boldsymbol{p}}(\boldsymbol{r})|\psi(t_f)\rangle|^2. \quad (8)$$

Then, the energy distribution, $g(E)$, can be converted from $f(p)$ according to

$$g(E) = \iint f(\boldsymbol{p})p\sin\theta\,d\theta\,d\varphi, \quad (9)$$

with θ and φ being the polar and azimuthal angles, respectively.

3. Results

3.1. Calculation of the ground state with the soft-core potential

We first test the convergence property of the calculation of the ground state at different values of softness parameter α. The (converged) first ionization potential I_p as a function of α, calculated with $\Delta x = 0.05$ a.u., is plotted in Fig. 1(a) for α in the range of 0.4–34. There are 10^3 grids for α used to get a smooth curve. As is expected, I_p varies monotonically with the change of α. The range of I_p covers the first ionization potentials of all atoms, from the largest one of He (0.904 a.u.) to the smallest one of Cs (0.143 a.u.). Thus, the value of α associated with any atom can be read from the curve, provided that the first ionization potential of this atom is known. For examples, it can be read from the curve that the α's corresponding to He, H, Ca, Na and Cs are 0.483, 2.0, 12.433, 18.282 and 33.641, respectively.

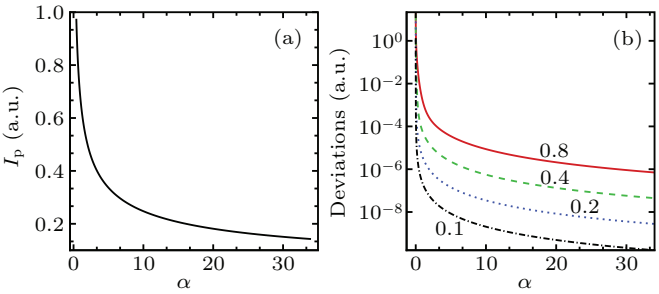


Fig. 1. (a) The first ionization potential I_p as a function of the softness parameter α ($\alpha = 0.4$–34), calculated with $\Delta x = 0.05$ a.u. (b) Deviations of I_p's calculated with $\Delta x = 0.1$, 0.2, 0.4 and 0.8 a.u. with respect to that obtained with $\Delta x = 0.05$ a.u. ($\alpha = 0.01$–34). Note the logarithmic scale in the vertical axis.

The Δx required for convergence is heavily dependent on the value of α, as is evidenced in Fig. 1(b), where deviations of I_p's calculated with $\Delta x = 0.1$, 0.2, 0.4 and 0.8 a.u. with respect to that obtained with $\Delta x = 0.05$ a.u. are shown for α in the range of 0.01–34. For large α, the deviations are rather small. The calculated ground state energy (as well as the wavefunction) converges fast with decreasing Δx. At very small α, however, the plotted deviations suddenly rise rapidly when α is decreased. Evidently, for very small α, $\Delta x = 0.1$ a.u. is far from sufficient to achieve convergence.

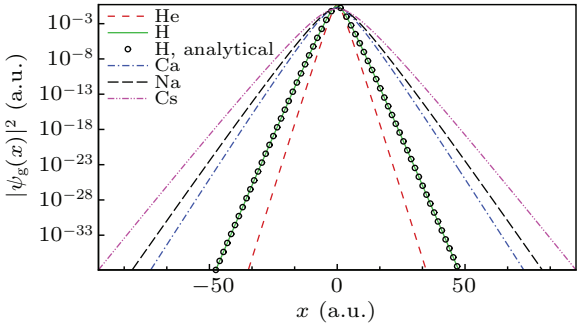


Fig. 2. Spatial electron distribution of the ground state, $|\psi_g(x)|^2$, for several atoms.

The value of the parameter α also measures the extent to which the ground state wavefunction, $\psi_g(x)$, is localized in space. The smaller the value of α, the more spatially localized the wavefunction $\psi_g(x)$; see Fig. 2, where we plot $|\psi_g(x)|^2$ against the coordinate x for atoms He, H, Ca, Na

and Cs, respectively. For comparison, we also plot the analytically obtained $|\psi_g(x)|^2$ for H (in circles). Excellent correspondence is found between the numerical and the analytical results. From the figure it can be seen that, when the vertical axis is in the logarithmic scale, all the curves shown are very close to straight lines except the parts around $x = 0$. The spatial extension of $\psi_g(x)$ is related to the property of the soft-core potential. When α is larger, the corresponding potential well is wider and shallower. Thus, its ability of binding the electron is weaker, leading to a more spatially extensive ground state wavefunction.

3.2. XUV pulses: perturbative regime

In the rest of the paper, only photoionization of atomic hydrogen (i.e., $\alpha = 2$) is discussed. We first study the photoionization by the XUV pulses with large photon energies in the perturbative regime. The carrier frequency of the pulse is chosen to be $\omega = 2$ a.u., and the total pulse duration $T_{\rm tot} = 30$ optical cycles. Photoelectron energy spectra are extracted from the 1D and 3D TDSE calculations performed at four typical peak laser intensities $I = 10^{12}$, 10^{13}, 10^{14}, and 10^{15} W/cm^2, and compared in Fig. 3. With these laser parameters, the ionization is dominated by the one-photon absorption process. To show the tiny signal of the multiphoton processes, logarithmic scale is used in the vertical axes of the spectra. A major difference between the 1D and 3D calculations is that, for all selected laser intensities, the photoelectron yields in the 3D case are more than an order of magnitude larger than in the 1D case. Because of the large photon energy (four times as large as the ionization potential of atomic hydrogen), excited states are scarcely populated during the ionization process and play little roles. Considering this, we extract the ionization probability by subtracting the final ground state population from unity. We find that, for each laser intensity, the ionization probability in the 3D calculation is around 74 times that in the 1D calculation. For a better comparison, we have rescaled each 1D spectrum by multiplying a factor (as denoted in the figure) equal to the ratio between the ionization probabilities from the 3D and 1D calculations. As can be seen in the figure, for all intensities, the one-photon peaks in the 1D and 3D spectra almost coincide with each other. Besides this, the general structures of the 1D spectra closely resemble those of the 3D spectra: they have similar envelopes and exhibit peaks at exactly the same energy positions. In each spectrum, the peak positions are separated by the photon energy. The fast oscillating parts of the spectra result as a consequence of the pulse shape. The evolution of the spectra with the intensity changes is also similar in the 1D and 3D cases. The ionization yield at the first peak is nearly proportional to the intensity in either the 1D or 3D calculation. At the second peak, the yield grows by about 100 times when the intensity increases by 10 times. The evolution of the spectra can be well explained in terms of perturbation theory: the electron yields at the n-photon absorption peaks scale with the laser intensities as I^n.

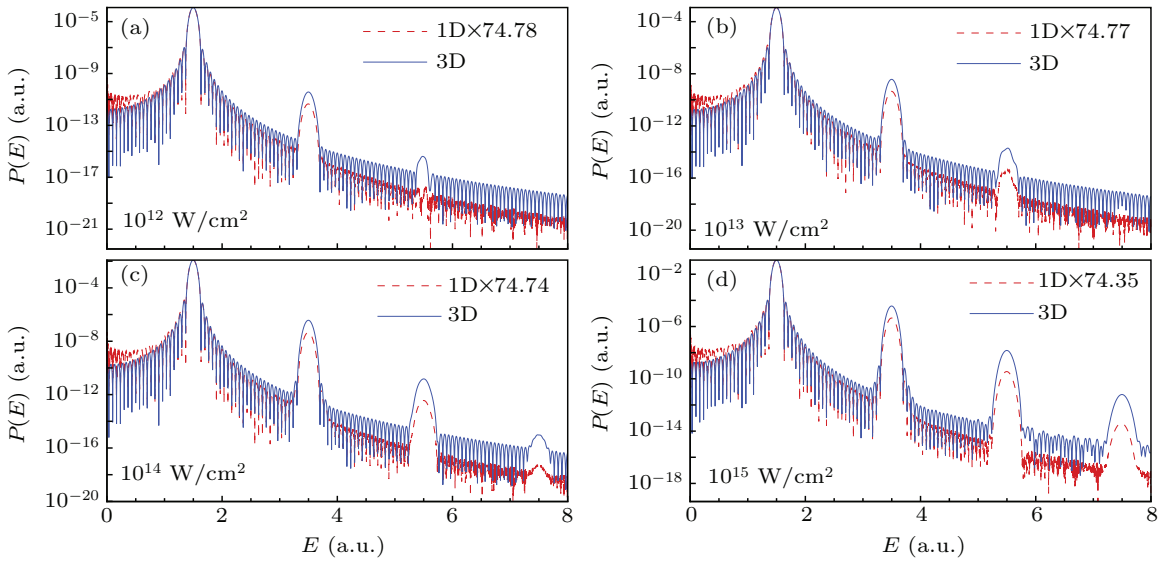


Fig. 3. Comparison of the photoelectron energy spectra obtained in the 1D and 3D TDSE calculations for a 30-cycle pulse with $\omega = 2.0$ a.u. at four different intensities 10^{12} W/cm^2 (a), 10^{13} W/cm^2 (b), 10^{14} W/cm^2 (c), 10^{15} W/cm^2 (d). The 1D spectra are rescaled by proper factors such that the one-photon absorption peaks of the 1D and 3D spectra have the same heights.

In addition to their similarities, the differences between the 1D and 3D spectra are also conspicuous. As mentioned before, the ionization probabilities from the 3D and 1D calculations are different by around 74 times, irrespective of the laser intensity. By checking the numerical data, it is found that, for any selected intensity, the ionization yield at the first peak from the 3D calculation is slightly more than 74 times that from the 1D calculation. The ratios between the ionization yields at the second peaks from the 3D and 1D calculations lie in the range of 615–621, which do not change much with

the intensity, either. For high-order peaks, the ratios become larger, but still intensity insensitive. The 1D calculation underestimates the ionization yield majorly because it underestimates the transition matrix elements between the ground and the continuum states. At $I = 10^{12}$ W/cm^2, the 3D spectrum exhibits three peaks, whereas the 1D spectrum has only two peaks: the three-photon absorption peak has not yet emerged, but appears as a small bump, hidden in the fast oscillating part of the spectrum. When the intensity is raised to 10^{13} W/cm^2, both spectra show three peaks. However, in the 3D case, the envelope of the curve shows an abrupt change around 7.5 a.u., which is probably due to the four-photon absorption, although the fourth peak does not show up. At intensities even higher, both spectra have four peaks. In our 3D calculations, we note that, if the density of the spatial grids is not sufficiently high, an additional peak would appear at about 6.5 a.u., which is actually the numerical artifact of unconvergent calculations.

3.3. XUV pulses: nonperturbative regime

When the intensity of the XUV pulses further increases, nonperturbative phenomena may occur. In recent years, it has been theoretically demonstrated that, when an atom is exposed to an intense high-frequency laser pulse, the ac Stark shift of the ground state would result in temporal interference of the emitted wavepackets, substantially modulating the spectrum.[11,12,43] This phenomenon is termed dynamic interference (DI).[43] To compare the DI patterns from the 1D and 3D calculations, we show in Fig. 4 the energy spectra computed at four laser intensities $I = 10^{17}$, 10^{18}, 2×10^{18}, and 3×10^{18} W/cm^2, for pulses of 30-cycle duration and $\omega = 2.0$ a.u. We do not choose intensities higher than 3×10^{18} W/cm^2 to avoid the possible influence of the nondipole effect of the laser-atom interaction. In Ref. [44], it was proved that, at $I = 4 \times 10^{18}$ W/cm^2, the nondipole effect is still relatively low, but at $I = 10^{19}$ W/cm^2, the nondipole effect is enormous. For a better view, the spectra from the 1D calculations have been rescaled by multiplying a factor of 10. The black vertical dashed lines denote energy positions of one-photon absorption peaks without taking account of the ac Stark effect, i.e., $\omega - I_p$, which is exactly 1.5 a.u.

The structures of the spectra shown could be interpreted in terms of the ac Stark shift and the ground state population, for which purpose, at every time step, we extract the instantaneous ground state energy and population. They are, respectively, calculated as the time-derivative of the phase of the projection amplitude of the wavefunction to the ground state, and the same projection amplitude squared; for details of the scheme, see Ref. [12]. Because of the fast oscillating laser field, the extracted energy and population are accordingly oscillating frequently with time; see, e.g., blue curves in Figs. 5(a) and 6(a), computed by solving the 1D TDSE at $I = 10^{17}$ W/cm^2. However, since the envelope of the pulse varies much slower than the oscillating laser field, one is usually only concerned about the response of the system averaged over the laser cycle,[12,44] which is related solely to the laser envelope. To get the cycle-averaged ac-Stark-shifted energy and electron population of the ground state, we employ the Fourier transformation filtering or the mean filtering to filter out the high-frequency oscillating components, arriving at smooth curves; see red curves in Figs. 5(a) and 6(a) against the blue ones. All curves other than the blue ones in Figs. 5 and 6 have been filtered.

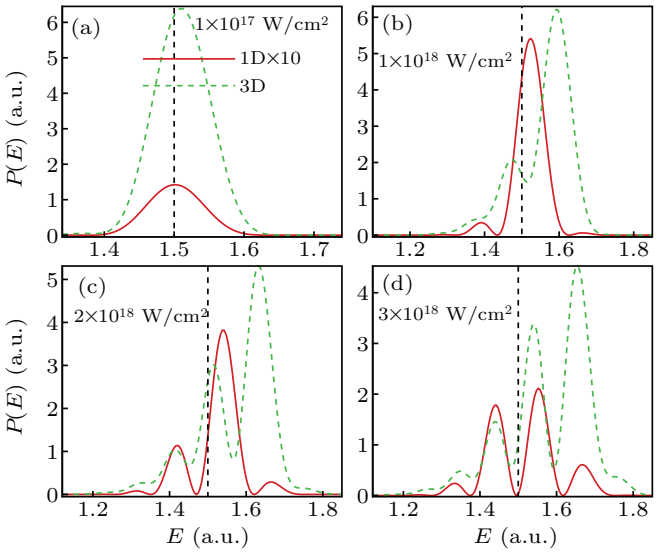


Fig. 4. Photoelectron energy spectra obtained at four different laser intensities 1.0×10^{17} W/cm^2 (a), 1.0×10^{18} W/cm^2 (b), 2.0×10^{18} W/cm^2 (c), 3.0×10^{18} W/cm^2 (d), for 30-cycle pulses of $\omega = 2.0$ a.u. Red lines: 1D calculations (rescaled by multiplying a factor 10). Green lines: 3D calculations. Vertical dashed lines: energy positions of ω–I_p, exactly 1.5 a.u.

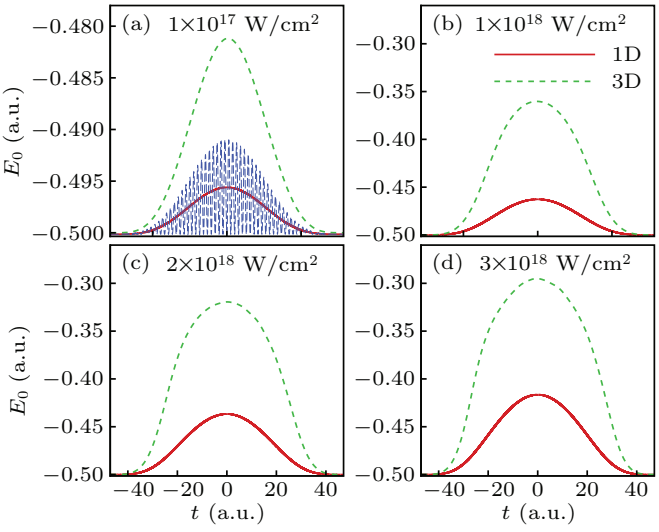


Fig. 5. Time dependence of the ac-Stark-shifted ground state energy at four different laser intensities 1.0×10^{17} W/cm^2 (a), 1.0×10^{18} W/cm^2 (b), 2.0×10^{18} W/cm^2 (c), 3.0×10^{18} W/cm^2 (d), for pulses of $\omega = 2.0$ a.u. and $T_{tot} = 30$ cycles. Red lines: 1D calculations. Green lines: 3D calculations. Blue line: 1D calculation without applying the filter (all other curves have been filtered).

We now return to the spectra (Fig. 4). At low intensity, $I = 10^{17}$ W/cm^2, both the spectra from the 1D and 3D calculations exhibit a single peak; no DI patterns are observed. This is because the ac Stark shift in each case is too tiny (less than 0.02 a.u.) to induce any observable interference to happen; see Fig. 5(a). However, the 1D and 3D calculations show differences: in addition to the large discrepancy between the peak heights, the peak positions also differ. The 1D peak lies at exactly 1.5 a.u., whereas the 3D one shifts to the right relative to 1.5 a.u. This shift is consistent with the corresponding Stark shift of the ground state. In the 1D case, however, the stark shift is less than 0.005 a.u., which can hardly result in any observable changes in the spectrum. When the laser intensity is raised to 10^{18} W/cm^2 [Fig. 4(b)], DI patterns emerge. Both spectra show two prominent subpeaks, one located at the right side of the vertical dashed line, the other at the left side. The ac Stark shift at this intensity is substantial [Fig. 5(b)], indicating the importance of large Stark shift for the appearance of DI. If the laser intensity is increased further, more interference subpeaks will emerge, the tallest peak shifting further to the right [Figs. 4(c)–4(d)]. As is expected, the ac Stark shift of the ground state also increases with the laser intensity.

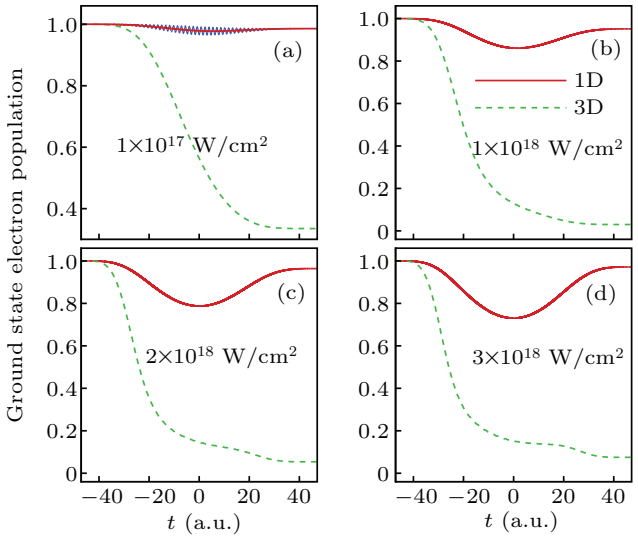


Fig. 6. Time dependence of the ground state electron population computed at four different laser intensities 1.0×10^{17} W/cm^2 (a), 1.0×10^{18} W/cm^2 (b), 2.0×10^{18} W/cm^2 (c), 3.0×10^{18} W/cm^2 (d), for pulses of $\omega = 2.0$ a.u. and $T_{\rm tot} = 30$ cycles. Red lines: 1D calculations. Green lines: 3D calculations. Blue line: 1D calculation without applying the filter (all other curves have been filtered).

The most notable difference between the 1D and 3D calculations is: in the 1D case, photoelectron signal almost approaches zero at the valleys of the spectra (corresponding to destructive interferences), whereas in the 3D case the signal at the valleys is still substantial. The higher contrast of the DI patterns and complete cancellations of the electron wavepackets emitted from the rising and falling edges of the pulses obtained in the 1D calculations can be explained in terms of the time-domain double-slit interference plus the time-varying ground state populations. Consider a pair of double slits (times) that result in destructive interference. In the 3D case, the electron population of the ground state at the second slit is largely depleted, much smaller than that at the first slit (see Fig. 6). The two electron wavepackets emitted at the two slits, respectively, have such different amplitudes that they cannot cancel each other completely. In the 1D case, however, as shown in Fig. 6, the ground state is largely populated at both the slits, for which reason both the corresponding wavepackets have large amplitudes, allowing for nearly complete cancellation.

3.4. The 400 nm pulses

We now turn to the TDSE calculations for pulses with a carrier wavelength of $\lambda = 400$ nm. The total pulse duration $T_{\rm tot}$ is chosen to be 10 optical cycles. Comparison between the 1D and 3D TDSE calculations for four different peak laser intensities $I = 1.7\times10^{12}$, 1.7×10^{13}, 1.7×10^{14}, 1.7×10^{15} W/cm^2 is presented in Fig. 7. When the photon energy is much smaller than the ionization potential, the ionization can be divided into two regimes in terms of the Keldysh parameter $\gamma = \sqrt{I_{\rm p}/2U_{\rm p}}$ ($U_{\rm p}$ is the ponderomotive energy), that is, the multiphoton regime for $\gamma \gg 1$, and the tunneling regime for $\gamma \ll 1$.[45] The value of γ for each intensity is given in the figure. Clearly, $I = 1.7\times10^{12}$ and 1.7×10^{13} W/cm^2 correspond to the deep multiphoton regime. The energy ranges of the spectra in Figs. 7(a) and 7(b) are set to be the same such that the separations between the main peaks are the same. The energy ranges are so chosen in order to show as many main peaks as possible. At the lowest intensity $I = 1.7\times10^{12}$ W/cm^2, the total ionization yield from the 1D calculation is about 6.7 times that from the 3D calculation. Both the 1D and 3D calculations produce two main peaks separated by the photon energy, each first main peak consisting of two subpeaks. We note that the two subpeaks in the 3D spectrum are located at slightly higher energies than their 1D counterparts. The second main peak in the 3D case is so weak that it is modulated by the frequent oscillations resulting from the pulse shape. The same modulation happens in the bump centered around 0.29 a.u. in the 1D spectrum, which is about to emerge as the third main peak. The oscillatory higher-energy parts of both curves are entirely due to the pulse shape. At $I = 1.7\times10^{13}$ W/cm^2, both the 1D and 3D curves have eight main peaks, the first six being smooth and the last two disturbed by the oscillations. The total ionization yield from the 1D calculation is around 8.7 times that from the 3D calculation. The ionization yields around the first four main peaks in the 1D spectrum are higher than those in the 3D spectrum, but the difference between them becomes smaller with increasing peak order. At the fifth main peaks, the ionization yield in the 3D case starts to exceed that in the 1D case.

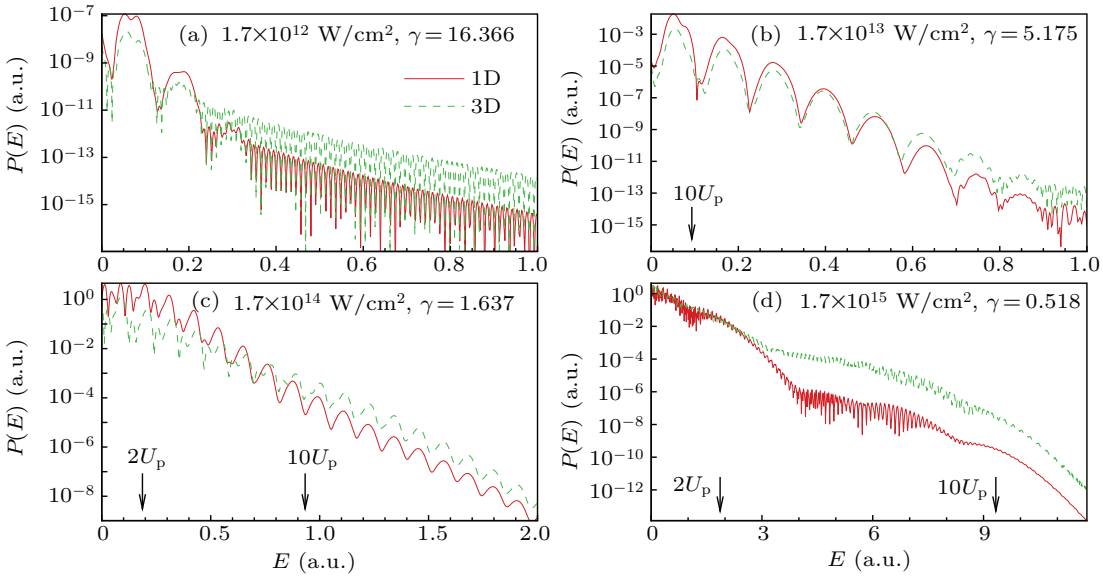


Fig. 7. Comparison of the photoelectron energy spectra obtained in the 1D and 3D TDSE calculations for pulses of $\lambda = 400$ nm and $T_{\rm tot} = 10$ cycles at four different intensities 1.7×10^{12} W/cm^2 (a), 1.7×10^{13} W/cm^2 (b), 1.7×10^{14} W/cm^2 (c), and 1.7×10^{15} W/cm^2 (d). The Keldysh parameter and, if possible, positions of $2U_{\rm p}$ and $10U_{\rm p}$ for each intensity are also given.

$I = 1.7\times10^{14}$ corresponds to the intermediate regime, but close to the multiphoton regime. The total ionization yield from the 1D calculation is about 6.2 times larger than the 3D result. As shown in Fig. 7(c), the spectra is composed of a multitude of main peaks. As the peak order increases, the ionization yield around a single main peak in the 3D spectrum gradually exceeds its 1D counterpart, similar to what happens in Fig. 7(b). In several low-order main peaks of both the curves, sharp subpeaks can be seen. These subpeaks become less sharp with increasing peak order and disappear in high-energy regions. It is worth noting that subpeaks in the 1D spectrum disappear earlier than in the 3D spectrum. When laser intensity is increased to 1.7×10^{15} W/cm^2, the tunneling regime is reached. The total ionization yield from the 3D calculation becomes larger than the 1D result, by approximately 10%. A notable phenomenon is that plateaus in both the 1D and 3D spectra emerge. While low-energy photoelectrons (up to $2U_{\rm p}$) escape from the atom directly without any revisit, the plateau electrons, propelled by the laser field, have recollided with the ionic core for different times. The cutoff energy of the plateau is $10U_{\rm p}$. We have denoted with arrows the positions of $2U_{\rm p}$ and $10U_{\rm p}$ for clarity. After $2U_{\rm p}$, both spectra show a rapid drop, followed by the plateaus. However, compared to the 3D spectrum, the 1D spectrum drops in a much wider energy range and to a much smaller value, such that the plateau appears later, and at a lower position.

For pulses of 400 nm or longer wavelength, the excited states are populated and play important roles in the ionization process. The 1D calculation gives the correct ground state energy. However, it cannot produce the real energy level structure. This is another reason, in addition to its misestimation of the transition matrix elements, why the 1D calculation produces higher or lower ionization yields at certain photoelectron energies for certain laser parameters.

3.5. The 800 nm pulses

Comparisons of the 1D and 3D TDSE calculations for 800 nm pulses with the total pulse duration of $T_{\rm tot} = 5$ optical cycles at four different peak laser intensities $I = 1.7\times10^{12}$, 1.7×10^{13}, 1.7×10^{14}, 1.7×10^{15} W/cm^2 are presented in Figs. 8(a)–8(d), respectively. As before, for each intensity, the Keldysh parameter is given in the figure. Whenever possible, energy positions of $2U_{\rm p}$ and $10U_{\rm p}$ are marked with the vertical arrows.

$I = 1.7\times10^{12}$ W/cm^2 corresponds to the deep multiphoton ionization regime. At this intensity, the total ionization probability from the 1D calculation is about 1.4 times the 3D result. The spectrum from the 1D calculation just shows one prominent main peak, while the second peak has yet to emerge (see the bump centered around 0.1 a.u.). The spectrum from the 3D calculation, however, has no pronounced main peaks at such low intensity. It only shows a bump around 0.04 a.u. Both spectra exhibit oscillatory structures at higher-energy regions, which are associated with the pulse shape. At the higher intensity, 1.7×10^{13} W/cm^2, the ionization roughly belongs to the multiphoton regime. Both of the 1D and 3D spectra have quite a few multiphoton peaks spaced by the photon energy. The total yield from the 1D calculation is as high as about 29 times that from the 3D calculation. When the intensity is increased to 1.7×10^{14} W/cm^2, the ionization becomes in the intermediate regime, but is close to the tunneling regime. The ratio between the yields from the 1D and 3D calculations is about 5.2. At this intensity, plateaus appear between $2U_{\rm p}$ and $10U_{\rm p}$ in both the 1D and 3D spectra. At low energies, the photoelectron signal (direct ionization) from the 1D calculation is much stronger than that from the 3D calculation. However, in

the plateau regions, the situation reverses: the 3D calculation gives much stronger signal of the rescattered electrons.

The highest selected intensity, 1.7×10^{15} W/cm^2, corresponds to the deep tunneling regime. At this intensity, the computational burden is quite large. In the 1D calculation, to make the calculation feasible, we adopt the method which projects the final state onto the scattering state. We set $\Delta x = 0.017$ a.u., $\Delta t = 0.00125$ a.u., and use a box of 6000 a.u. to get a converged spectrum. Because of the large cutoff energy of the plateau, $10U_p$, the number of grids in the momentum space needs to be rather large, which further make the computation more costly. In the obtained spectrum, the low-energy region and the plateau region are distinctly identified, both regions being composed of a large number of peaks. The envelope of the spectrum in these two regions exhibits oscillations; for a more clear view, see the inset in Fig. 8(d), where the spectrum segment bound by the dashed rectangle is enlarged. In the 3D calculation, it is easy to get a spectrum converged in the low-energy region (below $2U_p$). However, it is rather challenging for the plateau region to be converged. At present we have not yet get a converged result, but we show in the figure the spectrum obtained with the greatest possible effort. The radial box is chosen to be 4000 a.u., and the number of finite elements 4000; $\Delta t = 0.001$ a.u. and 200 partial waves are employed. Although unconverged in the high-energy region, the spectrum from the 3D simulation clearly shows the high-energy plateau, right between $2U_p$ and $10U_p$. Since the low-energy photoelectrons are dominant, we can roughly estimate the total ionization yield in the 3D calculation, which is found to be several percent higher than the 1D result.

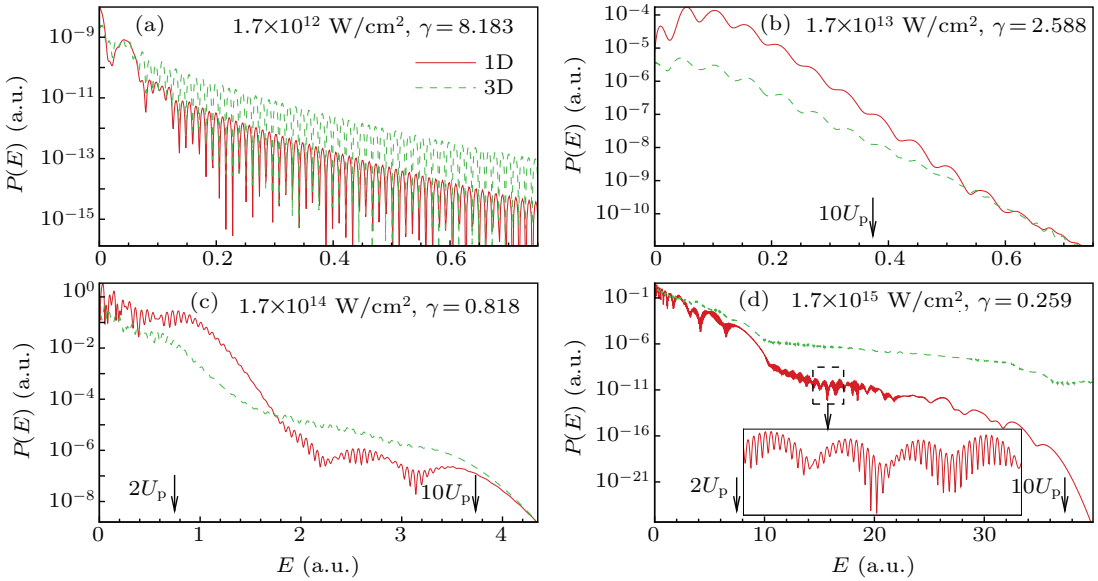


Fig. 8. Comparison of the photoelectron energy spectra obtained in the 1D and 3D TDSE calculations for pulses of $\lambda = 800$ nm and $T_{tot} = 5$ cycles at four different intensities 1.7×10^{12} W/cm^2 (a), 1.7×10^{13} W/cm^2 (b), 1.7×10^{14} W/cm^2 (c), and 1.7×10^{15} W/cm^2 (d). The Keldysh parameter and, if possible, positions of $2U_p$ and $10U_p$ for each intensity are also given. Inset in (d): enlarged view of the part of the spectrum encompassed by the dashed rectangle. The spectrum from the 3D calculation in (d) is not yet converged in the plateau region.

4. Summary

In summary, we have proposed a numerical scheme for solving the 1D TDSE, which employs several advanced technologies such as the wave-splitting technology and calculation of the spectra by projecting the wavefunction to the scattering state. To our knowledge, the latter has not been reported in the 1D TDSE calculation. We then systematically compare the photoelectron energy spectra for ionization of atomic hydrogen obtained by the proposed method employing the soft-core Coulomb potential with the precise 3D TDSE results. The comparison is carried out for pulses ranging from XUV to near infrared. For XUV pulses with photon energy far exceeding the ionization potential, two cases, one for intensities in the perturbative regime and the other in the nonperturbative regime, are discussed. For pulses of $\lambda \geqslant 400$ nm, where the photon energy is much smaller than the ionization potential, our discussion covers the multiphoton and tunneling regimes. While the 1D calculations can reproduce the general structures of the spectra from the 3D calculations, there are also many details that the 1D calculations fail to capture. The observed discrepancies can be mainly ascribed to the different transition matrix elements and energy level structures produced in the 1D and 3D calculations.

Our main findings include: (1) For XUV pulses in the perturbative regime, the 1D and 3D calculations produce electron spectra with similar envelopes and exactly the same peak positions. The 1D calculations largely underestimate the yield at any energies. (2) For XUV pulses in the nonperturbative regime, multipeak DI patterns are generated by both the 1D and 3D calculations, but with a sharp difference: near-zero electron signals at some valleys of the DI patterns are observed

in the 1D calculations, which are not found in the 3D calculations. (3) For pulses of $\lambda \geqslant 400$ nm in the multiphoton regime, both the 1D and 3D calculations produce typical spectra with multiphoton peaks. The peak positions show differences, and the total yield is usually larger in the 1D case than in the 3D case. In addition, with increasing peak order, the yield in the 3D case often gradually exceeds that in the 1D case. (4) For pulses of $\lambda \geqslant 400$ nm in the tunneling regime, both the 1D and 3D calculations produce the high-energy plateaus with similar cutoff energies. The plateau from the 3D calculation is usually higher than that from the 1D calculation.

References

[1] Krausz F and Ivanov M 2009 *Rev. Mod. Phys.* **81** 163
[2] Pazourek R, Nagele S and Burgdörfer J 2015 *Rev. Mod. Phys.* **87** 765
[3] Ueda K, Sokell E, Schippers S, Aumayr F, Sadeghpour H, Burgdörfer J, Lemell C, Tong X M, Pfeifer T, Calegari F, Palacios A, Martin F, Corkum P, Sansone G, Gryzlova E V, Grum-Grzhimailo A N, Piancastelli M N, Weber P M, Steinle T, Amini K, Biegert J, Berrah N, Kukk E, Santra R, Müller A, Dowek D, Lucchese R R, McCurdy C W, Bolognesi P, Avaldi L, Jahnke T, Schöffler M S, Dörner R, Mairesse Y, Nahon L, Smirnova O, Schlathölter T, Campbell E E B, Rost J M, Meyer M and Tanaka K A 2019 *J. Phys. B: At. Mol. Opt. Phys.* **52** 171001
[4] Walker B, Sheehy B, DiMauro L F, Agostini P, Schafer K J and Kulander K C 1994 *Phys. Rev. Lett.* **73** 1227
[5] Zhang L 2014 *Phys. Rev. Lett.* **112** 193002
[6] Chen Z, Liu F and Wen H 2019 *Chin. Phys. B* **28** 123401
[7] McPherson A, Gibson G, Jara H, Johann U, Luk T S, McIntyre I A, Boyer K and Rhodes C K 1987 *J. Opt. Soc. Am. B* **4** 595
[8] Huang Y Y, Lai X Y and Liu X J 2018 *Chin. Phys. B* **27** 73204
[9] Zuo R X, Song X H, Liu X W, Yang S D and Yang W F 2019 *Chin. Phys. B* **28** 94208
[10] Liu L, Zhao J, Yuan J M and Zhao Z X 2019 *Chin. Phys. B* **28** 114205
[11] Baghery M, Saalmann U and Rost J M 2017 *Phys. Rev. Lett.* **118** 143202
[12] Jiang W C and Burgdörfer J 2018 *Opt. Express* **26** 19921
[13] Wang N and Liu A 2019 *Chin. Phys. B* **28** 083403
[14] Jiang W C, Chen S G, Peng L Y and Burgdörfer J 2020 *Phys. Rev. Lett.* **124** 043203
[15] Xu Y and Bian X B 2020 *Chin. Phys. B* **29** 23202
[16] Brée C, Hofmann M, Demircan A, Morgner U, Kosareva O, Savel'ev A, Husakou A, Ivanov M and Babushkin I 2017 *Phys. Rev. Lett.* **119** 243202
[17] Xu L and Fu L 2019 *Phys. Rev. Lett.* **122** 253202
[18] Reed V C and Burnett K 1991 *Phys. Rev. A* **43** 6217
[19] Dörr M 2000 *Opt. Express* **6** 111
[20] Zhao J and Lein M 2013 *Phys. Rev. Lett.* **111** 043901
[21] de Aldana J V and Roso L 1999 *Opt. Express* **5** 144
[22] Kylstra N J, Worthington R A, Patel A, Knight P L, de Aldana J V and Roso L 2000 *Phys. Rev. Lett.* **85** 1835
[23] Javanainen J, Eberly J H and Su Q 1988 *Phys. Rev. A* **38** 3430
[24] Geltman S 2011 *J. At. Mol. Phys.* **2011** 573179
[25] Silaev A A, Ryabikin M Y and Vvedenskii N V 2010 *Phys. Rev. A* **82** 033416
[26] Majorosi S, Benedict M G and Czirják A 2018 *Phys. Rev. A* **98** 023401
[27] Gordon A, Santra R and Kärtner F X 2005 *Phys. Rev. A* **72** 063411
[28] Tian Y Y, Li S Y, Wei S S, Guo F M, Zeng S L, Chen J G and Yang Y J 2014 *Chin. Phys. B* **23** 053202
[29] Dziubak T and Matulewski J 2010 *Eur. Phys. J. D* **59** 321
[30] Rae S C, Chen X and Burnett K 1994 *Phys. Rev. A* **50** 1946
[31] Chen Y J, Liu J and Hu B 2009 *Phys. Rev. A* **79** 033405
[32] Yu H, Zuo T and Bandrauk A D 1998 *J. Phys. B: At. Mol. Opt. Phys.* **31** 1533
[33] Liu C, Nakajima T, Sakka T and Ohgaki H 2008 *Phys. Rev. A* **77** 043411
[34] Loudon R 1959 *Am. J. Phys.* **27** 649
[35] Schwengelbeck U and Faisal F H M 1994 *Phys. Rev. A* **50** 632
[36] Tong X M, Hino K and Toshima N 2006 *Phys. Rev. A* **74** 031405
[37] Wang S, Jiang W C, Tian X Q and Sun H B 2020 *Phys. Rev. A* **101** 053417
[38] Jiang W C, Tong X M, Pazourek R, Nagele S and Burgdörfer J 2020 *Phys. Rev. A* **101** 053435
[39] Rescigno T N and McCurdy C W 2000 *Phys. Rev. A* **62** 032706
[40] Rayson M J 2007 *Phys. Rev. E* **76** 026704
[41] Schneider B I and Collins L A 2005 *J. Non-Cryst. Solids* **351** 1551
[42] Jiang W C and Tian X Q 2017 *Opt. Express* **25** 26832
[43] Demekhin P V and Cederbaum L S 2012 *Phys. Rev. Lett.* **108** 253001
[44] Wang M X, Liang H, Xiao X R, Chen S G, Jiang W C and Peng L Y 2018 *Phys. Rev. A* **98** 023412
[45] Keldysh L V 1965 *Sov. Phys. JETP* **20** 1307